Fast and low-temperature (70 °C) mineralization of ink-jet printed mesoporous TiO2 photoanodes using ambient air plasma

Tomáš Homola[*a], Petr Dzik[b], Michal Veselý[b], Jakub Kelar[a], Mirko Černák[a], Martin Weiter[b]

[a] R&D Center for Low-Cost Plasma and Nanotechnology Surface Modifications (CEPLANT), Department of Physical Electronics, Faculty of Science, Masaryk University, Kotlářská 267/2, 611 37 Brno, Czech Republic

[b] Faculty of Chemistry, Brno University of Technology, Purkyňova 118, 612 00 Brno, Czech Republic

ABSTRACT: Hybrid mesoporous titania/silica electron-generating and transporting layers were prepared using wet-coating with a dispersion consisting of prefabricated titania nanoparticles and a methyl-silica binder. Titania/methyl-silica wet layers were deposited by ink-jet printing and further mineralized by low-temperature atmospheric–pressure air plasma using diffuse coplanar surface barrier discharge (DCSBD) to form a titania/silica hybrid nanocomposite coating. Morphological analysis performed by scanning electron microscopy revealed no damage to the titania nanoparticles and chemical analysis performed by X-ray photoelectron spectroscopy disclosed a rapid decrease in carbon and increase in oxygen, indicating the oxidation effect of the plasma. The coatings were further electrochemically investigated with linear sweep voltammetry and chronoamperometry. The magnitude of photocurrent and photocatalytic activity were found to increase significantly with the plasma exposure in the order of 10's of seconds. The results obtained demonstrate the potential of DCSBD ambient air plasma for fast and low-temperature mineralization of titania mesoporous coatings.

1. INTRODUCTION

Irradiated photoanodes containing a conductor/n-type semiconductor interface[1] have been extensively used as core components in several promising photo-electrochemical systems applicable to radiative energy harvesting, environmental remediation, sensing and other fields. Dye-sensitized solar cells (DSSC)[2], in which the photo-electrochemical system typically relies upon a mesoporous TiO2 layer coated with photosensitizer dye, have emerged as promising low-cost photovoltaic technology in recent years and constitute the most notable application field for semiconducting photoanodes. Other suitable applications for semiconducting photoanodes involve, for example, electro-assisted photocatalytic treatment of water[3], hydrogen production by water splitting[4] and various sensing systems[5]. Titanium dioxide is the most popular semiconducting material to be employed for the purposes under discussion; however a number of other transition metal oxides have attracted considerable attention as well. Titania photoelectroactive layers have been successfully deposited by a number of techniques both in gas and liquid phases. The deposition of liquid precursor formulations by some of the many wet-coating methods[6] is popular, since the equipment required is relatively simple and there is a high degree of compatibility with ambient conditions. Moreover, these techniques are intrinsically suited to roll-to-roll processing and when modified printing techniques are employed (e.g. gravure, flexo- or screen printing), direct patterning of the printed layers is easily achieved. The coating formulations may contain various types of titania as the sole non-volatile component and various functional additives are often included in order to improve the properties of both the liquid formulation and the resulting layer. However, natural or forced drying of the wet-coated layers rarely produces coatings with satisfactory performance and some fixing or curing process therefore needs to be employed. Thermal sintering is the most straightforward approach to consolidating a wet-coated titania layer. Fine mesoporous TiO2 films are usually cured at high temperatures by means of a slow convection heating procedure (at least 30 min above 350 °C) in order reliably to remove all organic components present in the coating formulation. The high sintering temperature, however, precludes the use of such a procedure for thermally sensitive substrates and results in performance deterioration in transparent conducting oxide substrates. Alternative approaches to interconnecting the TiO2 particles with a porous film without high temperature sintering have therefore come to attract close attention. Investigations into the matter have therefore shifted their focus towards, for example, organic-binder-free pastes, UV irradiation, and laser sintering[7–9].

H. Kim et al.[10] employed titanium isopropoxide as a binder for low-temperature consolidation of TiO2 nanoparticles. Even though the dip-coating method was used sev-

eral times to deposit layers of sufficient thickness, the entire coating had to be processed in an oven at 120 °C for 1 hour, which is quite a long time if roll-to-roll processing is envisaged. Similarly, Y.F. Jiang et al.[11] used the doctor-blade technique to deposit an N-La co-doped TiO_2 photoanode, which had to be further processed at 120 °C for 30 min to eliminate volatiles – still an extended period for convenient roll-to-roll processing. Silica has been successfully employed as a binder for passive photo-catalytic coatings[12] and, despite its inherently insulating nature, it has proved useful for titania photoanodes as well[13]. H. Lee[14] employed an atmospheric-pressure electro-spraying process to deposit hierarchically structured TiO_2. The deposition process was followed by a low-temperature chemical post-treatment that took several hours. H.W. Chen[15] used an electrophoretic approach to depositing TiO_2 mesoporous coatings but this method does not meet the requirements of large-area applications. J. Wang et al.[16] used a nanocomposite of graphene and TiO_2 in a perovskite solar cell. The graphene-TiO_2 was prepared by spin-coating and heated at 150 °C for an hour. A.K. Chandiran et al.[17] deposited ultra-thin 15-nm crystalline TiO_2 using atomic layer deposition (ALD), at 200 °C, onto a pre-fabricated mesoporous SiO_2 matrix; although their power conversion efficiency reached 7.1%, the SiO_2 was fabricated in a series of multiple high-temperature steps. Furthermore, there are currently two major drawbacks to the successful deployment of ALD in large-area, fully integrated, roll-to-roll systems: i) While recently published pioneering work[18] on plasma-enhanced atmospheric pressure ALD shows promise for large-area roll-to-roll solar cell manufacture, ALD is essentially a vacuum process and therefore not appropriate to in-line roll-to-roll processes; ii) ALD deposition times are still prohibitively long; it took approx. 25 min to deposit a 15-nm layer, for example. Other contributions refer to binder-free TiO_2: in Yune et al.[19] and Lin et al.[20], as in the previous examples, the coating was annealed at low temperature for 2 hours[19] and 30 min[20], respectively. Very recently, C. Wu et al.[21] fabricated firm TiO_2 photoanodes at low temperature using a blend of commercial high-temperature and low-temperature pastes obtained from Solaronix. Their photovoltaic performances were, however, limited by low electron transport and inadequate light-harvesting efficiency.

The above summary of the state of the art indicates that although binder-free options for semiconducting photoanode fabrication have been the subjects of considerable attention, it has become apparent that an approach based on utilizing binder-containing formulations processed by a swift and more logistically appropriate curing method may deliver results far superior in terms of both electrical and mechanical properties.

Electrical plasmas possess the unique capacity of producing oxidative species at high densities and low gas temperatures at the same time as maintaining high uniform reaction rates over relatively large areas. Consequently, plasma sintering or plasma mineralization of the organic binder in titania nanoparticulate coatings is a highly competitive and viable low-temperature approach to the manufacture of mesoporous TiO_2 films[22–24]. Of particular practical interest is low-temperature (less than ~ 200 °C) plasma sintering, using an open air plasma that eliminates the need for expensive and cumbersome chambers such as those employed to lower pressure and control gas mixtures. Very recently, Zen et al.[25] developed a low-temperature annealing technique with TiO_2 photoelectrodes, based on annealing at 150 °C under UV light irradiation for 18 h followed by 5 minutes of treatment in ambient air plasma generated by a volume dielectric barrier discharge. Such combined sintering may be applicable to plastic substrates, but total sintering times in the order of hours are far too long for practical applications, particularly if a roll-to-roll mass production of flexible DSSCs [26] is required.

A diffuse coplanar surface barrier discharge (DCSBD) plasma source (Roplass s.r.o., Czech Rep.) has the capacity to generate diffuse high-density "cold" plasmas in ambient air, N_2 H_2, H_2O and other low-cost plasma working gases in a way that permits in-line, low-cost modification of the surface nanolayers of large-area substrates such as glass, metals, polymer fabrics and films[27,28]. Ambient air DCSBD plasma has been successfully tested for fast low-temperature calcination of metalorganic nanofibers[29].

In this study, diffuse high-density ambient air plasma generated by DCSBD was employed for the mineralization of hybrid titania/silica layers which had been prepared by wet-coating onto various substrates a dispersion containing prefabricated titania nanoparticles and a recently-reported organosilica binder. The suspension was deposited by inkjet material printing, facilitating precise control over coating thickness and shaping. A range of experimental techniques were employed to monitor the progress of binder mineralization, so the evolution of important material properties could thus be followed and investigated in detail.

2. EXPERIMENTAL

2.1 Materials

Printing of titania layers was performed with an experimental Fujifilm Dimatix 2831 ink-jet printer, the benefits of which have repeatedly and convincingly been demonstrated both for patterning titania[30–32] and for other functional materials[33–35]. The materials and procedures employed for the printable suspension formulation were optimized in advance: a recently-developed organo-silica binder[36] was adopted without modification and mixed with commercial nanoparticulate titania (Evonik P25) in a range of ratios. The resulting formulations were used to print samples of variable topology, depending on the experimental technique anticipated. Based on a preliminary screening phase, the mineralization effect of the plasma was expected to be strongly dependent on layer thickness and porosity. Two titania formulations were therefore chosen from a portfolio of titania printable pastes developed in the course of previous work[37].

The first printable titania ink was denoted 9AD, prepared by mixing 4 mL of stock organosilica binder solution (20 wt.% in anhydrous ethanol) with 4 mL of stock titania dispersion (20 wt.% in Dowanol PM solvent) and 8 mL of isobutanol. Approx. 2 cm³ of 1 mm glass balls were combined with this in a 20 mL glass vial and it was placed overnight on an oscillating lab shaker set to 1000 rpm. This ball-milling step, although improvised, proved surprisingly effective. It results in the disintegration of larger titania aggregates and ensures reliable jetting through the 20-μm nozzle orifices of the printer. The printing ink was freshly prepared before use by mixing the ball-milled formulation with an equal volume of n-hexanol, providing acceptable wetting behaviour on the substrate types used in the study. Thus the solid loading of the printing ink was 5 wt.% and the titania/binder ratio was 50:50. The samples prepared with this ink were overprinted three times in order to prepare thick, dense, strongly-adhering coatings, then denoted 9AD-3L.

The second ink was denoted 10AD, prepared in exactly the same way, except that a solution of 6 mL of titania stock dispersion was mixed with 2 mL of binder stock solution, giving a titania/binder ratio of 75:25. All other procedures were identical to those used in the previous case, but only a single layer was printed with this formulation, resulting in thin, fluffy, highly porous and mechanically rather delicate coatings, then denoted 10AD-1L.

2.2 Plasma treatment

The atmospheric-pressure ambient air plasma was generated by surface dielectric barrier discharge (sDBD) with coplanar configuration of electrodes: diffuse coplanar surface barrier discharge (DCSBD). DCSBD is based on the DBD principle, in which dielectric-covered electrodes are powered by high-voltage AC current, typically at frequencies of between 10 and 500 kHz – sufficient to create an active discharge region. Whereas most DBD plasmas are of volume configuration (plane-parallel electrode and counter-electrode), DCSBD utilizes coplanar geometry of electrodes, like that of AC plasma displays. In contrast to even the most modern coplanar DBD plasmas, DCSBD is capable of generating plasmas of much higher uniformity and power density (up to 100 W.cm⁻³), although the plasma layer is only 0.3 mm thick and visually diffuse. At the operation parameters employed, the vibrational and rotational temperatures in plasma, determined by optical emission spectroscopy, are 2645 ± 195 K and 377 ± 18 K, respectively[38]. The rotational temperature was calculated from the OH band and may be interpreted as an upper limit for the neutral gas temperature in the plasma in the circumstances. The overall temperature of the gas is lower, and close to 70 °C. DCSBD is described in more detail in Homola et al.[27] and Černák et al.[38].

2.3 Surface analysis

The surface morphology of coatings was studied by means of a Mira3 scanning electron microscope (Tescan, Czech Rep.). The images, at 200 kx magnification, were captured at 8 kV accelerating voltage and 3 mm working distance The TiO₂ coatings were analysed on FTO glass samples. Specific surface and porosity properties were investigated directly by the nitrogen sorption method performed with Quantachrome Autosorb iQ system on bulk powder samples obtained by drying the liquid printing compositions, and also indirectly by ellipsometric measurements performed on the printed and processed layers with a Jobin-Yvon UVISEL 2 spectroscopic ellipsometer.

X-ray diffractometry (XRD) was used to measure the crystalline properties of the TiO₂ films. The spectra were acquired with a 1.542Å Cu Kα SmartLab (Rigaku, Japan) diffractometer in Bragg-Brentano geometry. The Scherrer equation was used to calculate TiO₂ anatase/rutile crystallite sizes. The coatings were analysed on 1-mm-thick soda-lime glass slides.

FTIR spectroscopy was employed for direct monitoring of the residual methyl group depletion by plasma treatment. This process manifests as a significant decrease in, and ultimately the disappearance of, characteristic peaks corresponding to the vibrations of the methyl moieties in the binder (2831–3006 cm⁻¹). The broad signal peaking at 3300 cm⁻¹ can be assigned to the vibrations of hydroxyl moieties present in the hydrolysed and condensed binder. Apparently, the employed plasma treatment did not influence it at all.

Further evidence of the nature and extent of the binder mineralization was obtained by X-ray photoelectron spectroscopy (XPS) using an Al Kα ESCALAB 250Xi (ThermoFisher Scientific). All samples were measured at one spot (650 μm) at a take-off angle of 90° in 10⁻⁸ mbar vacuum at 20 °C. An electron flood-gun was used to compensate for charges on sample surfaces. The spectra were referenced to Ti2p at 458.8 eV.

Linear sweep voltammetry and chronoamperometry were employed for indirect investigation of the extent of binder mineralization. As shown recently[37], raw unprocessed layers of nanocrystalline titania bonded with methyl-silica binder have very poor charge transfer and charge-generating properties. However, these improve substantially when the organic moieties of the binder are removed by oxidation. Thus it becomes possible to follow the degree of binder conversion in the plasma-treated layer by monitoring the photocurrent generated in irradiated samples deposited on an electrically-conductive substrate[39].

Photoelectrochemical characterization was performed by linear sweep voltammetry at room temperature using a two-electrode setup with 1 cm² titania patches. The printed FTO slide was scratched to create two isolated FTO strips. One strip, with the printed titania patch, served as the working electrode and the opposite, naked, FTO strip as the counter-electrode. This setup was fitted into a custom-built quartz cuvette, which was filled with a 0.1 M aqueous solution of perchloric acid and fitted onto an optical bench equipped with a UV-A lamp emitting a broad peak centred at 365 (Sylvania Lynx-L 11 W). A magnetic stirrer was placed beneath the cuvette and a magnetic flea within it provided efficient electrolyte mixing.

The lamp emission was monitored with a Gigahertz Optic X97 irradiance meter with a UV-3701 probe with the irradiance set to 2 mW/cm² by adjusting the lamp-to-cuvette distance. Measurements of the photocurrents generated were taken with an electrometer built on the basis of an NI Labview platform supplying a linear voltage gradient of 10 mV/s from -0.5 to 2 V.

Further indirect evidence of the extent of binder mineralization was obtained by means of a photocatalytic experiment. The printed layers (20 × 20 mm squares on microscope slides) were immersed in a 1E-4 molar aqueous solution of coumarine. The ROS generated on the surface of the photocatalyst upon UV-A irradiation oxidizes coumarine into its hydroxylated derivatives, some of which give off strong fluorescence, peaking at 460 nm[40]. This method has attracted considerable attention as a possible tool for swift and simple evaluation of photo-catalyst activity[41], but in this case it was used solely for the evaluation of photocatalytic activity changes resulting from the plasma treatment.

## 3. RESULTS AND DISCUSSION

3.1 Structural analysis

Figure 1 presents the scanning electron microscopy images of titania mesoporous coatings with two distinct formulation: 9AD-3L and 10AD-1L, containing 50:50 and 75:25 titania/methyl-silica binder respectively. Reference (plasma-untreated) 9AD-3L and 10AD-1L coatings appear in **Figure 1a** and **Figure 1b** respectively. The structure of the two coatings is very similar and shows that homogeneity and meso- and macro-porosity are all high. The titania nanoparticles are approximately 20–25 nm in diameter and glued together, which resulted in structures with diameter of 40–50 nm. The size of the pores varied between 50 and 250 nm in both coatings. The difference between 9AD-3L and 10AD-1L was minor; however the shape of the titania nanoparticles was slightly more distinguishable in the 10AD-1L coating, which tallies with its lower concentration of organic methyl-silica binder. **Figures 1c** and **1d** show the effects of plasma mineralization on the morphology of the 9AD-3L and 10AD-1L samples. There is no notable difference between the plasma-mineralized samples and references, so it appears that the plasma had no effect on morphological structure; this evidence arises out of the plasma being of a temperature too low to lead to damage or deformation effects.

The specific surface, its porosity and pore-size distribution are important material texture parameters directly influencing chemical activity. While their determination for bulk material is straightforward, using the nitrogen sorption method and the associated BET theory[42], the measurements become more complex for thin, porous layers due to the prohibitively low ratio of active material mass to that of the glass substrate. Therefore, specific surface was analyzed for the bulk starting titania powder and bulk powders of both titania-binder mixes used in this study prior to thin layer deposition and plasma treatment. It emerged that the specific surface of the starting bulk titania was 48 m²/g, a value that tallied closely with the supplier's data. The value dropped to 12 and 36 m²/g for powders obtained by drying 9AD and 10AD compositions respectively. This arose out of partial blockage of accessible pores by the binder and is naturally greater for the more binder-rich 9AD formulation.

Further investigation of textural changes in the actual printed layers before and after processing was performed indirectly by evaluation of SEM images and ellipsometric spectra of the inkjet-printed samples before and after plasma processing. A complex multilayer model involving a variable void layer, adapted from our previous work on the optical properties of printed pure titania films[43], was used for the recorded spectra fitting. This facilitated a relative comparison of porosity changes upon plasma treatment. In neither case was any significant systematic change detected after plasma processing.

The real specific surface of the processed layer (expressed as accessible surface area per geometrical footprint surface area, i.e. the roughness factor) may be estimated from the value of the specific surface determined for bulk powder and the known weight coverage of the substrate, which was approx. 0.3 mg/cm² for 9AD-3L and 0.1 mg/cm² for 10AD-1L. The roughness factor proved equal for both formulations, at a value 36 (12 m²/g × 0.3 mg/cm² = 36 = 36 m²/g × 0.1 mg/cm²). The lower specific surface of the 9AD formulation (12 m²/g) was compensated by greater surface loading (0.3 mg/cm²); however, this assumption is based solely on weight balance and does not take other effects into account. It should therefore be considered with a degree of caution. It can be maintained with more confidence, on the other hand, that the accessibility of pores and cavities in 9AD coating, which are located deeper in the layer, was certainly limited in comparison to the 10AD coating.
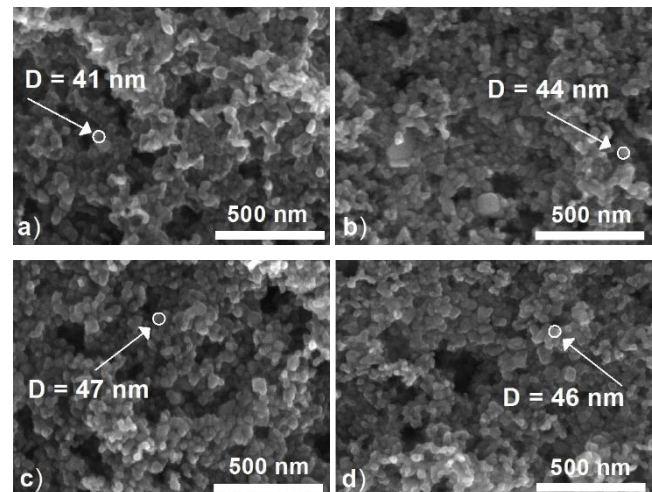
Figure 1. SEM images of a) 9AD-3L reference; b) 10AD-1L reference; c) 9AD-3L 64 s plasma-treated; and d) 10AD-3L 64 s plasma-treated samples.

The thickness of the coatings was evaluated from the profilometric measurements that appear in **Figure 2:**

9AD-3L was approx. 800 nm thick and 10AD-1L approx. 300 nm. The 9AD-3L coating that had been prepared with a titania/binder ratio of 50:50 (ink overprinted three times) was approximately three times thicker than 10AD-1L and exhibited an RMS height of 0.71 μm ± 0.05 μm. The thinner 300 nm 10AD-1L coating was of a deviation that indicated that the pores were smaller. Printing patterns were observed in 1AD-1L coating whereas thicker 9AD-3L showed higher macro-homogeneity due to larger pores.
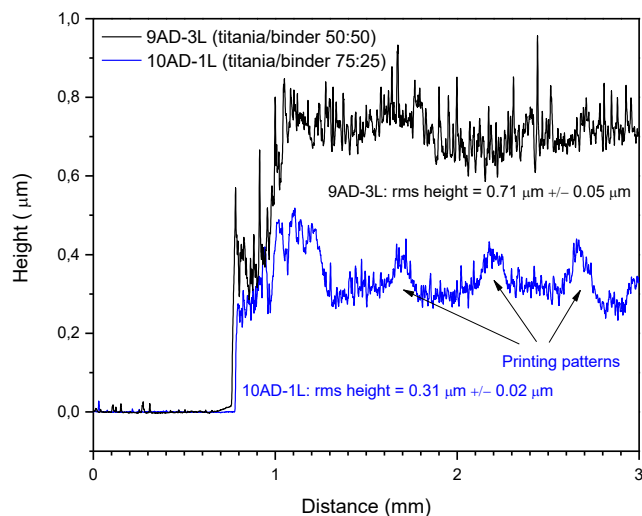

Figure 2. Thickness of the coatings and their rms heights.

XRD analysis (**Figure S1†, Supporting Information**) showed that both coatings consist of anatase and rutile. The sizes of the anatase grains for both 9AD-3L and 10AD-1L are very similar, e.g. the strongest peak (101) anatase measured 23 and 26 nm for 9AD-3L and 10AD-1L respectively. No effect on the crystalline structure of either coating after the longest plasma treatment (64 seconds) was observed. The XRD findings correlate closely with the SEM morphological scans and it is clear that structures observed by SEM are anatase crystals at various orientations glued with binder. On the other hand, the organic methyl silica binder was of amorphous structure, since no characteristic silicon peak appeared in XRD spectra. The spectra were significantly influenced by silica from the soda-lime glass substrate.

3.2 Chemical analysis

Figures 3a and **3b** present the evolution over time of FTIR absorbance spectra of titania coatings of both the types studied after plasma treatment. The spectra clearly reflect the major difference between the 9AD-3L and 10AD-1L samples, i.e. their thickness. Naturally, the thicker 9AD-3L coating exhibited stronger absorbance than the thinner 10AD-1L coating. The changes after plasma treatment for 2–64 s in the region of interest at 2831–3006 cm^{-1}, corresponding to asymmetrical and symmetrical stretching of –CH$_3$ (2850, 2920 and 2970 cm^{-1}), appear subtle and less significant in 9AD-3L. Nevertheless, **Figure 4** shows the –CH$_3$ peak area calculated with the appropriate baseline; the signal decrease is clearly apparent. The thicker

9AD-1L coating showed a swift drop in peak area during the first few seconds of plasma treatment, which corresponds with surface oxidation of the accessible methyl groups. Any further effect is limited, as plasma cannot effectively penetrate the interior of the thicker, compact and binder-rich coating. Similarly, a swift initial drop in CH$_3$ peak area was observed for 10AD-3L coating, but in this case the process of plasma oxidation continued evenly throughout the range of treatment times because the plasma penetrated through the porous structure deep into the whole coating.

a)

b)
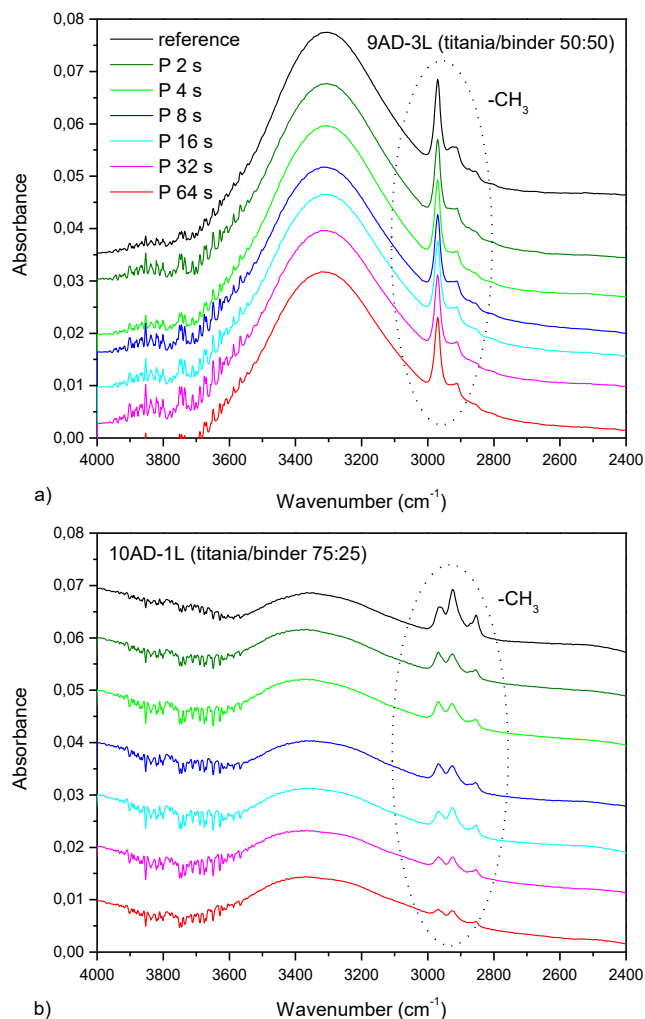
Figure 3. FTIR transmission spectra of a) 9AD-3L and b) 10AD-1L samples treated in plasma for 2-64 seconds.

Both plasma-treated coatings were further evaluated by XPS. **Table 1** shows the concentration of elements on the surface of the 9AD-3L and 10AD-1L coatings. The main difference between coatings appears in the concentrations of carbon, titanium and silicon. Whereas the 9AD-3L reference sample exhibited 28.8 at.% carbon, 3.5 at.% titanium and 21.3 at.% silicon, the reference sample with a 10AD-1L coating showed a lower concentration of carbon, 21.6 at.%; higher titanium, 9.3 at.% and lower silicon, 16.5 at.%. The low concentration of sodium comes from the surface of the glass and confirms a high level of porosity,

since XPS clearly detected a signal from the substrate. This leads to the conclusion that the data acquired are influenced by silicon oxide from the glass, which contributes to the signal from the binder in the coating.
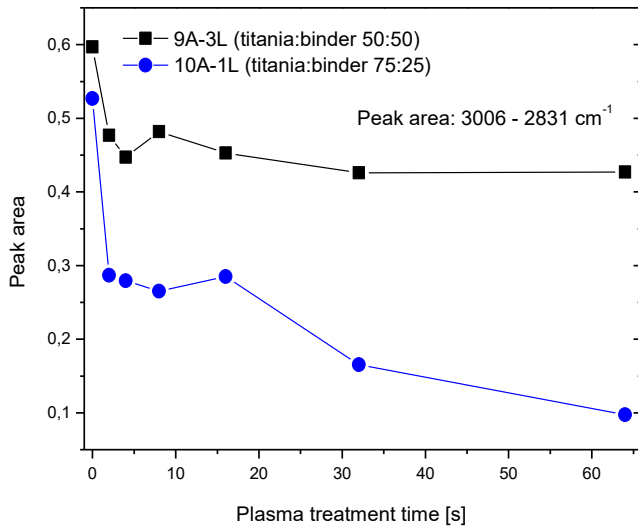
Figure 4. Evolution of 3006 – 2831 cm-1 peak area with plasma treatment time for 2-64 seconds for 9AD-3L and 10AD-1L samples.

The lower concentration of carbon and silicon in the 10AD-1L coating accords with the initial difference between the coatings; 9AD-3L had a lower proportion of titania in the organic methyl-silica binder portion (50:50) whereas 10AD-1L had a higher proportion of titania in organic methyl-silica binder (75:25). The 9AD-3L exhibited a Ti/Si ratio of 0.17, which was very low, whereas 10AD-1L gave a significantly higher Ti/Si ratio of 0.56. Both coatings, 9AD-3L and 10 AD-1L, had similar, almost stoichiometric, TiO_2/SiO_2 composition with O/(Ti+Si) ratios of 1.81 and 1.95, respectively.
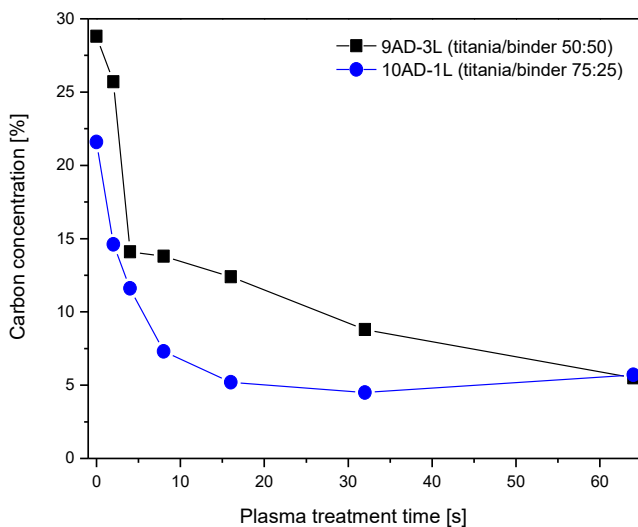
Figure 5. Evolution of overall carbon concentration for 9AD-3L and 10AD-1L samples treated in plasma for 2–64 seconds.

Table 1. Concentration of elements as detected by XPS for 9AD-3L and 10AD-1L samples treated in plasma for 2-64 seconds.

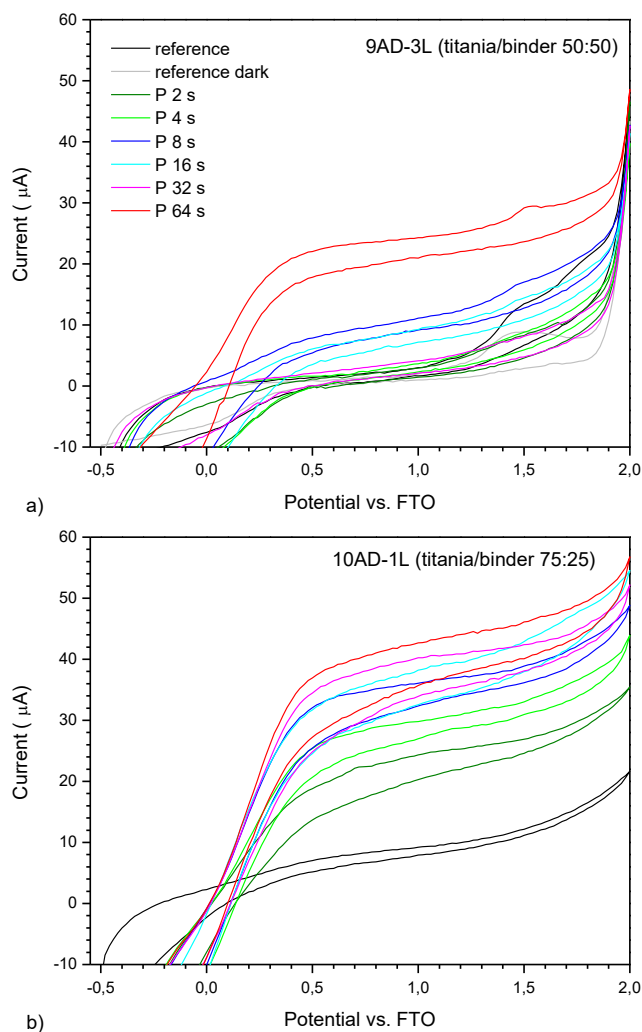| Sample	Concentration of elements						
	C_{1s} [%]	O_{1s} [%]	Ti_{2p} [%]	Si_{2p} [%]	Na_{1s} [%]	Ti/Si	O/(Ti+Si)
9AD-3L							
Ref.	28.8	44.8	3.5	21.3	1.5	0.17	1.81
P 2 s	25.7	51.3	3.3	16.8	2.8	0.19	2.56
P 4 s	14.1	59.3	4.4	20.5	1.6	0.21	2.39
P 8 s	13.8	59.9	4.0	20.8	1.5	0.19	2.43
P 16 s	12.4	60.4	4.2	21.7	1.2	0.19	2.34
P 32 s	8.8	62.7	3.7	23.5	1.3	0.16	2.31
P 64 s	5.5	66.2	3.3	23.5	1.5	0.14	2.37
10AD-1L							
Ref.	21.6	50.3	9.3	16.5	2.3	0.56	1.95
P 2 s	14.6	58.2	9.3	14.4	3.4	0.64	2.46
P 4 s	11.6	62.4	9.1	15.1	1.0	0.60	2.58
P 8 s	7.3	64.4	9.7	15.5	3.0	0.63	2.56
P 16 s	5.2	65.1	10.0	16.4	3.1	0.61	2.46
P 32 s	4.5	65.9	10.5	16.1	2.8	0.65	2.48
P 64 s	5.7	65.0	9.5	16.6	2.9	0.57	2.48

Plasma mineralization for 2–64 seconds led to a decrease in atomic carbon concentration, as shown in **Figure 5**. The manner in which carbon decrease took place is similar for both coatings, differing only in initial atomic carbon concentration, apparently higher for the 9AD-3L coating with the higher proportion of binder. Plasma treatments led to a steady decrease of carbon concentration while plasma treatment for 64 s yielded the same values of carbon concentration in both, approx. 5–6 at.%. This is clearly saturation for carbon removal, which is also influenced by the limitations of ex-situ XPS. The plasma treatment had no effect on overall concentration of titanium and silicon and their ratios changed only slightly (0.15–0.20 for 9AD-1L and 0.55–0.65 for 10AD-3L) with plasma treatment time. The removal of carbon was accompanied by oxidation processes; a higher amount of oxygen was detected as plasma treatment time increased. Since the carbon signal decreased rapidly, further analysis of the C_{1s} high resolution peak was rendered opaque by low signal.

Analysis of the high-resolution Si_{2p} peak (**Figure S2**†) showed that it shifted towards higher binding energy after plasma treatment. Plasma mineralization for 64 seconds led to a shift of the Si_{2p} peak towards higher binding energies due to a decrease in the R-SiO$_x$ component that is characteristic of the organic silicon-containing binder[36]. However, the shift towards higher energy may be associated with oxygen attached to the silicon atom forming SiO_2. High-resolution Ti_{2p} peaks (**Figure S3**†) in 9AD-3L showed no noticeable changes
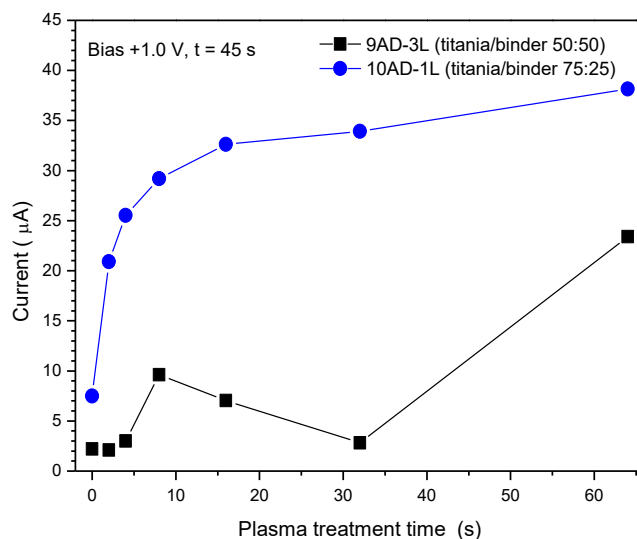
after the plasma treatments; it can be assumed that the oxidation process largely involved the silicon in the methyl-silica organic binder and led to breaking of Si–C bonds. This could be specifically confirmed by C1s analysis (not shown here); however, C–Si and C–C/C–H are energet-ically similar (284.5 eV and 284.8 eV, respectively) and the C1s peak showed an overall decrease of signal for both characteristic binding energies.

### 3.3 Electrochemical characterization

The coatings were further characterized by linear sweep voltammetry to investigate the electrochemical properties induced in them by plasma treatment. Cyclic linear sweep voltammograms of the 9AD-3L and 10AD-1L coatings appear in **Figures 6a** and **6b** respectively. In both coatings, plasma treatment led to a steady increase of photocurrent magnitude with plasma treatment time. This trend was independently confirmed by a separate chrono-amperometric measurement at +1V bias, shown in **Figure 7**.

Figure 7. Photocurrent evolution with plasma treatment time for 2-64 s for 9AD-3L and 10AD-1L samples.

Figure 6. Cyclic linear sweep voltametric curves for a) 9AD-3L and b) 10AD-1L samples treated in plasma for 2-64 s.
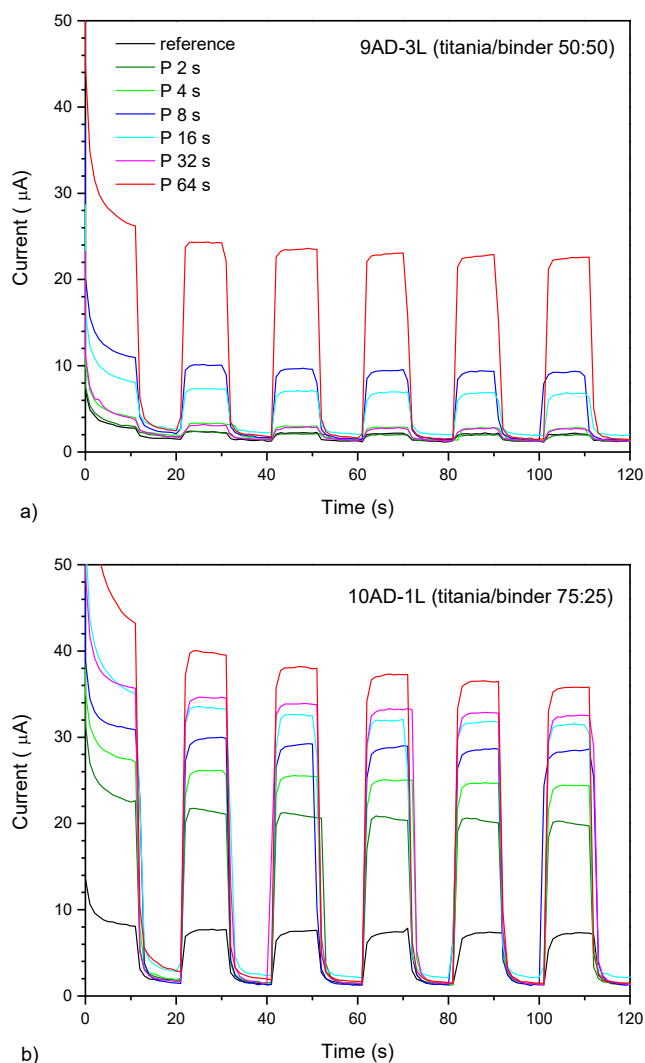

Figure 8. Chronoamperometric records with period of 10 s for a) 9AD-3L and b) 10AD-1L samples treated in plasma for 2-64 s.

Photocurrent values originating from the chrono-amperometric measurement of 9AD-3L and 10AD-1L coatings are further summarized in **Figures 8a** and **8b** respectively, where the photocurrent evolution appears as a function of plasma mineralization time. A significant difference in behaviour was observed and its relation to the layer structure can be explained: the thin, porous 10AD-1L layer undergoes a quick initial surface binder oxidation followed by slower in-depth mineralization taking place through the pores. Extensive binder oxidation results in a major increase of layer conductivity manifested as increasing photocurrent values. On the other hand, plasma penetration into the thick, dense layers of the 9AD-3L type is limited and therefore binder mineralization takes place only on the surface, which is reflected in generally lower photocurrent values.

3.4 Consequences for photocatalytic activity

The results of photocatalytic activity testing, using a coumarin fluorescent probe, with untreated and plasma-treated 9AD-1L and 10AD-3L coatings, are shown in **Figures 9a** and **9b**, respectively. The figures show the coumarin concentration profiles together with kinetic parameters obtained from a simplified sequential reaction model (coumarine → 7-hydroxycoumarin → further oxidized intermediates), as recommended for this situation by Cernigoj et al.[41]. Although the magnitude of the differences is not high, they are consistent and further illustrate the processes taking place upon plasma-induced binder mineralization. A significant difference in the initial rate of 7-hydroxy coumarin generation emerged between the 9AD-3L (i.e. the more binder-rich, less porous) and the 10AD-1L (i.e. less binder, more porous) coatings. The more porous and binder-deficient coating produced significantly faster initial rates, so it may be posited that high porosity and low binder content, associated with more exposed photocatalyst grains, are more important to photocatalytic activity than layer thickness and post-deposition processing. In any event, for both layer types, an appreciable acceleration of the initial reaction rate was observed after plasma mineralization of the binder. The difference is subtle in the case of 9AD-3L-type layers, as only a thin surface modification is taking place. This is consistent with the behaviour of this sample type in other experiments. On the other hand, the acceleration is much more pronounced in 10AD-1L-type samples (i.e. thin, porous) as a deeper effect of plasma processing is enabled by the porous nature of the layer. Worth noting is the slightly sigmoidal shape of the fluorescence traces for the unprocessed, thin, porous layer types: at the very start, the initial reaction rate is quite slow; it then accelerates during the reaction proper as the binder becomes further mineralized by the photocatalytic effect contributed by the irradiated photocatalyst. This explanation has been demonstrated by repeated experiments with a single plasma-untreated slide. In the course of five reaction runs, the activity of such a slide constantly increased until it finally matched that of plasma-treated slides.

a)

b)
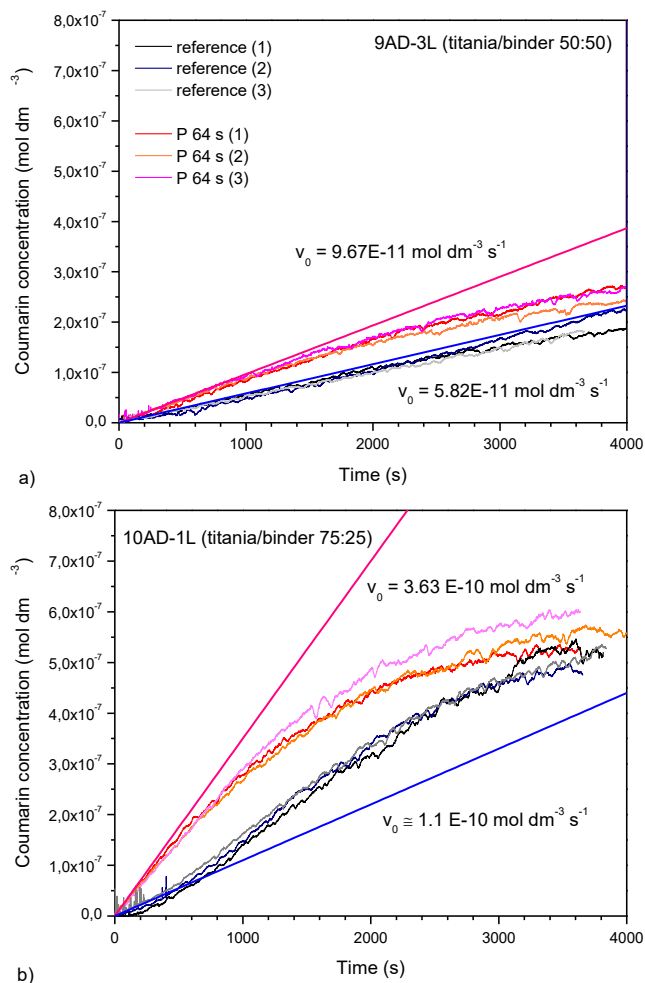
Figure 9. Photocatalytic activity expressed with raw fluorescence signal of oxidized fluorescent probe n-hydroxycoumarin plotted against reaction time for a) 9AD-3L and b) 10AD-1L samples treated in plasma for 64 s.

3.5 Efficiency of the plasma treatment

The results of XPS demonstrated that the way in which the chemical changes took place in both coatings induced by plasma mineralization were similar. XPS detects information mainly from the top surface, and its sensitivity penetrates only a few nm below the surface. However, the sensitivity can significantly vary for porous films, as was confirmed in this study by the presence of sodium in XPS spectra that could only have originated from the glass substrate. The concentration of sodium measured in the 9AD-3L coating was almost twice as low as that in 10AD-1L coating, indicating loss of ejected photoelectrons from the glass substrate due to the longer path in the thicker 9AD-3L coating. Therefore XPS is not limited to only the first few nm below the surface; it can also detect changes deeper in the coating.

The photocatalytic activity induced by plasma treatment differs significantly between thicker 9AD-3L and thinner 10AD-1L coatings. Apart from higher efficiency of photocatalytic activity in thinner 10AD-1L coating, because of higher content of titania, the depth to which particles

from plasma penetrate effectively into the coating is interesting. Although the plasma-chemical nature of the mineralization process is not fully understood, the predominantly high energetic states of nitrogen and oxygen could induce such effective changes in coating structure leading to desorption of methyl groups. The possible mechanism has been exhaustively addressed by M.R. Baklanov et. al[44], who posit that the chemical reaction between the oxygen radical and Si–CH3 groups starts with detachment of hydrogen and further reaction with another oxygen atom leads to complete loss of the methyl group and formation of surface-active sites capable of chemisorption of water molecules, forming Si–H and Si–OH[45,46]. Replacement of non-polar –CH3 groups with polar –OH groups leads to increases in dielectric constant[47]. In microelectronics, this is often considered an undesirable effect when low-k dielectrics are processed by plasma[48,49]. Conversely, in this work, an increase in dielectric constant may well lead to higher capacity in the silica surface, which could further contribute to explanation of the higher photocurrents that appear in Figs. 6-8.

Recent papers have also described the use of plasma for the preparation of TiO_2 porous films in solar-cell applications. A nitrogen atmospheric-pressure plasma jet has been employed to sinter printed TiO_2 films for 600 s[23]. A clear drawback of plasma jet in small-area treatment is associated with the substantially high temperature of 500 °C involved. Such a level of heat in the process is currently a limiting parameter in the fabrication of solar cells and other optoelectronic devices, since it is incompatible with low-cost, lightweight, flexible plastic materials, which are unable to withstand high temperatures.

H Jung et al.[50] used large-area atmospheric pressure plasma to remove organic binders from TiO_2 films. The plasma was operated by 13.56 MHz discharge in Ar/O_2 at 120 W, where the active plasma area was 1.1 cm × 1.5 cm. The temperature in plasma was 190 °C, sufficiently low to enable the use of plastic substrates and permit manufacture in roll-to-roll fashion. S. Zen el al.[25] very recently published a study of low-temperature fabrication of TiO_2 films by ambient air dielectric barrier discharge[51]. The process temperature was 150 °C, which clearly showed that dielectric barrier discharges are preferable for low-temperature manufacture of functional TiO_2 coatings.

This study employed DBD with coplanar configuration of electrodes and obtained similar results for plasma effect on TiO_2 films. In contrast to the plasma sources used in other contributions[23,25,50], DCSBD can provide a much larger area for treatment at lower temperatures. This difference clearly arises out of the coplanar configuration of the electrodes, which generates only a thin layer of plasma with ultra-high power density while the gas temperature remains low, at 70 °C.

4. CONCLUSIONS

This contribution presents a method for the fabrication of mesoporous TiO_2 photoanodes using cold 70 °C plasma in ambient air. TiO_2 photoanodes were created on FTO/glass substrates and TiO_2 coating on plain glass slides. The low-temperature DCSBD plasma mineralization was capable of efficiently removing the organic moieties of binder while preserving the mesoscopic structure of TiO_2. The extent of the mineralization depends on the layer porosity, thickness and is satisfactory even in the more challenging case of thick, compact titania coatings. When compared with standard thermal sintering or UV curing, the DCSBD plasma mineralization provides a number of significant advantages: thermal sintering produces a well-sintered and fully mineralized coating but is inappropriate for flexible polymeric substrates due to the high processing temperatures involved. Moreover, the super-hydrophobic nature of thermally sintered titania/silica layers predicates further hydrophilization. UV curing appears to be an attractive low-temperature option, but the process is prohibitively slow for practical use. The plasma process reported herein is capable of producing highly photoelectroactive titania coatings at very fast curing times.

While a number of studies and/or commercial products targeting the same general goal, i.e. fabrication of highly active photoanodes featuring a transition metal oxide semiconducting layer, have appeared recently, the process reported herein features several important advantages over them. Firstly, the novel organosilica binder present in the formulation also acts as an efficient stabilizing agent for the suspended titania nanoparticles. Thus a low viscosity ink with a high solid loading was obtained, furthermore boasting excellent shelf-life and ink-jet printability with a potential for essentially unlimited patterning and scaling options. The thickness of the printed layer can be adjusted on a wide scale by altering the printer settings and/or overprinting more layers and the texture (i.e. porosity and specific surface) may, to a certain extent, be adjusted by changing the titania-binder ratio. Secondly, the binder acts as a "mortar", gluing the deposited nanoparticles together after its mineralization and the processed layer thus features improved adhesion and overall stability over the course of mechanical stress and wear. Thirdly, the plasma mineralization process provides production performance superior to the previously-considered processes (thermal sintering and UV curing), taking only a fraction of the time required for them at far lower temperatures, making it particularly suitable for incorporation into roll-to-roll fabrication units. It could constitute a major step forward in the large-scale manufacture of flexible solar cells, among many other applications.

ASSOCIATED CONTENT

AUTHOR INFORMATION

Corresponding Author

*E-mail: tomas.homola@mail.muni.cz, (T. Homola),
Tel: +420 549 49 4974

REFERENCES

(1) Kumar, S. G.; Devi, L. G. Review on Modified TiO2 Photocatalysis under UV/Visible Light: Selected Results and Related Mechanisms on Interfacial Charge Carrier Transfer Dynamics. *J. Phys. Chem. A* **2011**, *115* (46), 13211–13241.

(2) Gong, J.; Liang, J.; Sumathy, K. Review on Dye-Sensitized Solar Cells (DSSCs): Fundamental Concepts and Novel Materials. *Renewable Sustainable Energy Rev.* **2012**, *16* (8), 5848–5860.

(3) Butterfield, I. M.; Christensen, P. A.; Hamnett, A.; Shaw, K. E.; Walker, G. M.; Walker, S. A.; Howarth, C. R. Applied Studies on Immobilized Titanium Dioxide Films Ascatalysts for the Photoelectrochemical Detoxification of Water. *J. Appl. Electrochem.* **1997**, *27* (4), 385–395.

(4) Alexander, B. D.; Kulesza, P. J.; Rutkowska, I.; Solarska, R.; Augustynski, J. Metal Oxide Photoanodes for Solar Hydrogen Production. *J. Mater. Chem.* **2008**, *18* (20), 2298–2303.

(5) Yang, M.; Li, L.; Zhang, S.; Li, G.; Zhao, H. Preparation, Characterisation and Sensing Application of Inkjet-Printed Nanostructured TiO2 Photoanode. *Sens. Actuators, B* **2010**, *147* (2), 622–628.

(6) Krebs, F. C. Fabrication and Processing of Polymer Solar Cells: A Review of Printing and Coating Techniques. *Sol. Energy Mater. Sol. Cells* **2009**, *93* (4), 394–412.

(7) Fu, N.; Huang, C.; Liu, Y.; Li, X.; Lu, W.; Zhou, L.; Peng, F.; Liu, Y.; Huang, H. Organic-Free Anatase TiO$_2$ Paste for Efficient Plastic Dye-Sensitized Solar Cells and Low Temperature Processed Perovskite Solar Cells. *ACS Appl. Mater. Interfaces* **2015**, *7* (34), 19431–19438.

(8) Di Giacomo, F.; Zardetto, V.; D'Epifanio, A.; Pescetelli, S.; Matteocci, F.; Razza, S.; Di Carlo, A.; Licoccia, S.; Kessels, W. M. M.; Creatore, M.; Brown, T. M. Flexible Perovskite Photovoltaic Modules and Solar Cells Based on Atomic Layer Deposited Compact Layers and UV-Irradiated TiO$_2$ Scaffolds on Plastic Substrates. *Adv. Energy Mater.* **2015**, *5* (8), 1401808.

(9) Kim, H.; Auyeung, R. C. Y.; Ollinger, M.; Kushto, G. P.; Kafafi, Z. H.; Piqué, A. Laser-Sintered Mesoporous TiO2 Electrodes for Dye-Sensitized Solar Cells. *Appl. Phys. A: Mater. Sci. Process.* **2005**, *83* (1), 73–76.

(10) Kim, H.; Hwang, T. Effect of Titanium Isopropoxide Addition in Low-Temperature Cured TiO2 Photoanode for a Flexible DSSC. *J. Sol-Gel Sci. Technol.* **2014**, *72* (1), 67–73.

(11) Jiang, Y. F.; Chen, Y. Y.; Zhang, B.; Feng, Y. Q. N, La Co-Doped TiO2 for Use in Low-Temperature-Based Dye-Sensitized Solar Cells. *J. Electrochem. Soc.* **2016**, *163* (10), F1133–F1138.

(12) Shibata, H.; Sakai, H.; Rangsunvigit, P.; Hirano, T.; Abe, M. Preparation and Photocatalytic Activity of Titania Particulate Film with Silica as Binder. *Surf. Coat. Int., Part B* **2003**, *86* (2), 125–130.

(13) Králová, M.; Dzik, P.; Kašpárek, V.; Veselý, M.; Cihlář, J. Cold-Setting Inkjet Printed Titania Patterns Reinforced by Organosilicate Binder. *Molecules* **2015**, *20* (9), 16582–16603.

(14) Lee, H.; Hwang, D.; Jo, S. M.; Kim, D.; Seo, Y.; Kim, D. Y. Low-Temperature Fabrication of TiO$_2$ Electrodes for Flexible Dye-Sensitized Solar Cells Using an Electrospray Process. *ACS Appl. Mater. Interfaces* **2012**, *4* (6), 3308–3315.

(15) Chen, H.-W.; Liang, C.-P.; Huang, H.-S.; Chen, J.-G.; Vittal, R.; Lin, C.-Y.; Wu, K. C.-W.; Ho, K.-C. Electrophoretic Deposition of Mesoporous TiO2 Nanoparticles Consisting of Primary Anatase Nanocrystallites on a Plastic Substrate for Flexible Dye-Sensitized Solar Cells. *Chem. Commun.* **2011**, *47* (29), 8346–8348.

(16) Wang, J. T.-W.; Ball, J. M.; Barea, E. M.; Abate, A.; Alexander-Webber, J. A.; Huang, J.; Saliba, M.; Mora-Sero, I.; Bisquert, J.; Snaith, H. J.; Nicholas, R. J. Low-Temperature Processed Electron Collection Layers of Graphene/TiO2 Nanocomposites in Thin Film Perovskite Solar Cells. *Nano Lett.* **2014**, *14* (2), 724–730.

(17) Chandiran, A. K.; Yella, A.; Stefik, M.; Heiniger, L.-P.; Comte, P.; Nazeeruddin, M. K.; Grätzel, M. Low-Temperature Crystalline Titanium Dioxide by Atomic Layer Deposition for Dye-Sensitized Solar Cells. *ACS Appl. Mater. Interfaces* **2013**, *5* (8), 3487–3493.

(18) van den Bruele, F. J.; Smets, M.; Illiberi, A.; Creyghton, Y.; Buskens, P.; Roozeboom, F.; Poodt, P. Atmospheric Pressure Plasma Enhanced Spatial ALD of Silver. *J. Vac. Sci. Technol., A* **2015**, *33* (1), 01A131.

(19) Yune, J. H.; Karatchevtseva, I.; Triani, G.; Wagner, K.; Officer, D. A Study of TiO2 Binder-Free Paste Prepared for Low Temperature Dye-Sensitized Solar Cells. *J. Mater. Res.* **2012**, *28* (3), 488–496.

(20) Lin, L.-Y.; Lee, C.-P.; Tsai, K.-W.; Yeh, M.-H.; Chen, C.-Y.; Vittal, R.; Wu, C.-G.; Ho, K.-C. Low-Temperature Flexible Ti/TiO2 Photoanode for Dye-Sensitized Solar Cells with Binder-Free TiO2 Paste. *Prog. Photovoltaics* **2012**, *20* (2), 181–190.

(21) Wu, C.; Chen, B.; Zheng, X.; Priya, S. Scaling of the Flexible Dye Sensitized Solar Cell Module. *Sol. Energy Mater. Sol. Cells* **2016**, *157*, 438–446.

(22) Chang, H.; Hsu, C.-M.; Kao, P.-K.; Yang, Y.-J.; Hsu, C.-C.; Cheng, I.-C.; Chen, J.-Z. Dye-Sensitized Solar Cells with Nanoporous TiO2 Photoanodes Sintered by N2 and Air Atmospheric Pressure Plasma Jets With/without Air-Quenching. *J. Power Sources* **2014**, *251*, 215–221.

(23) Chang, H.; Yang, Y.-J.; Li, H.-C.; Hsu, C.-C.; Cheng, I.-C.; Chen, J.-Z. Preparation of Nanoporous TiO2 Films for DSSC Application by a Rapid Atmospheric Pressure Plasma Jet Sintering Process. *J. Power Sources* **2013**, *234*, 16–22.

(24) Dembele, A.; Rahman, M.; MacElroy, J. M. D.; Dowling, D. P. Evaluation of Microwave Plasma Sintering for the Fabrication of Dye Sensitized Solar Cell (DSSC) Electrodes. *J. Nanosci. Nanotechnol.* **2012**, *12* (6), 4769–4774.

(25) Zen, S.; Inoue, Y.; Ono, R. Low Temperature (150 °C) Fabrication of High-Performance TiO2 Films for Dye-Sensitized Solar Cells Using Ultraviolet Light and Plasma Treatments of TiO2 Paste Containing Organic Binder. *J. Appl. Phys.* **2015**, *117* (10), 103302.

(26) Søndergaard, R.; Hösel, M.; Angmo, D.; Larsen-Olsen, T. T.; Krebs, F. C. Roll-to-Roll Fabrication of Polymer Solar Cells. *Mater. Today* **2012**, *15* (1), 36–49.

(27) Homola, T.; Matoušek, J.; Kormunda, M.; Wu, L. Y. L.; Černák, M. Plasma Treatment of Glass Surfaces Using Diffuse Coplanar Surface Barrier Discharge in Ambient Air. *Plasma Chem. Plasma Process.* **2013**, *33* (5), 881–894.

(28) Černák, M.; Kováčik, D.; Ráheľ, J.; Sťahel, P.; Zahoranová, A.; Kubincová, J.; Tóth, A.; Černáková, Ľ. Generation of a High-Density Highly Non-Equilibrium Air Plasma for High-Speed Large-Area Flat Surface Processing. *Plasma Phys. Controlled Fusion* **2011**, *53* (12), 124031.

(29) Medvecká, V.; Kováčik, D.; Zahoranová, A.; Stupavská, M.;

Černák, M. Atmospheric Pressure Plasma Assisted Calcination of Organometallic Fibers. *Mater. Lett.* **2016**, *162* (3), 79–82.

(30) Morozova, M.; Kluson, P.; Krysa, J.; Dzik, P.; Vesely, M.; Solcova, O. Thin TiO2 Films Prepared by Inkjet Printing of the Reverse Micelles Sol–gel Composition. *Sens. Actuators, B* **2011**, *160* (1), 371–378.

(31) Černá, M.; Veselý, M.; Dzik, P.; Guillard, C.; Puzenat, E.; Lepičová, M. Fabrication, Characterization and Photocatalytic Activity of TiO2 Layers Prepared by Inkjet Printing of Stabilized Nanocrystalline Suspensions. *Appl. Catal., B* **2013**, *138*, 84–94.

(32) Dzik, P.; Veselý, M.; Kete, M.; Pavlica, E.; Štangar, U. L.; Neumann-Spallart, M. Properties and Application Perspective of Hybrid Titania-Silica Patterns Fabricated by Inkjet Printing. *ACS Appl. Mater. Interfaces* **2015**, *7* (30), 16177–16190.

(33) Hynek, J.; Kalousek, V.; Žouželka, R.; Bezdička, P.; Dzik, P.; Rathouský, J.; Demel, J.; Lang, K. High Photocatalytic Activity of Transparent Films Composed of ZnO Nanosheets. *Langmuir* **2014**, *30* (1), 380–386.

(34) Vidmar, T.; Topič, M.; Dzik, P.; Opara Krašovec, U. Inkjet Printing of Sol–gel Derived Tungsten Oxide Inks. *Sol. Energy Mater. Sol. Cells* **2014**, *125*, 87–95.

(35) Dzik, P.; Veselý, M.; Neumann-Spallart, M. Inkjet Printed Interdigitated Conductivity Cells with Low Cell Constant. *ECS J. Solid State Sci. Technol.* **2016**, 5 (7), P412–P418.

(36) Grégori, D.; Benchenaa, I.; Chaput, F.; Thérias, S.; Gardette, J.-L.; Léonard, D.; Guillard, C.; Parola, S. Mechanically Stable and Photocatalytically Active TiO 2 /SiO 2 Hybrid Films on Flexible Organic Substrates. *J. Mater. Chem. A* **2014**, *2* (47), 20096–20104.

(37) Králová, M.; Dzik, P.; Kašpárek, V.; Veselý, M.; Cihlář, J. Cold-Setting Inkjet Printed Titania Patterns Reinforced by Organosilicate Binder. *Molecules* **2015**, *20* (9), 16582–16603.

(38) Černák, M.; Černáková, L.; Hudec, I.; Kováčik, D.; Zahoranová, A. Diffuse Coplanar Surface Barrier Discharge and Its Applications for in-Line Processing of Low-Added-Value Materials. *Eur. Phys. J. Appl. Phys.* **2009**, *47* (2), 22806.

(39) Morozova, M.; Kluson, P.; Dzik, P.; Vesely, M.; Baudys, M.; Krysa, J.; Solcova, O. The Influence of Various Deposition Techniques on the Photoelectrochemical Properties of the Titanium Dioxide Thin Film. *J. Sol-Gel Sci. Technol.* **2013**, *65* (3), 452–458.

(40) Ishibashi, K.; Fujishima, A.; Watanabe, T.; Hashimoto, K. Detection of Active Oxidative Species in TiO2 Photocatalysis Using the Fluorescence Technique. *Electrochem. commun.* **2000**, *2* (3), 207–210.

(41) Černigoj, U.; Kete, M.; Štangar, U. L. Development of a Fluorescence-Based Method for Evaluation of Self-Cleaning Properties of Photocatalytic Layers. *Catal. Today* **2010**, *151* (1–2), 46–52.

(42) Horikawa, T.; Katoh, M.; Tomida, T. Preparation and Characterization of Nitrogen-Doped Mesoporous Titania with High Specific Surface Area. *Microporous Mesoporous Mater.* **2008**, *110* (2), 397–404.

(43) Schmiedova, V.; Dzik, P.; Vesely, M.; Zmeskal, O.; Morozova, M.; Kluson, P. Optical Properties of Titania Coatings Prepared by Inkjet Direct Patterning of a Reverse Micelles Sol-Gel Composition. *Molecules* **2015**, *20* (8), 14552–14564.

(44) Baklanov, M. R.; de Marneffe, J.-F.; Shamiryan, D.; Urbanowicz, A. M.; Shi, H.; Rakhimova, T. V.; Huang, H.; Ho, P. S. Plasma Processing of Low-K Dielectrics. *J. Appl. Phys.* **2013**, *113* (4), 41101.

(45) Shoeb, J.; Wang, M. M.; Kushner, M. J. Damage by Radicals and Photons during Plasma Cleaning of Porous Low-K SiOCH. I. Ar/O2 and He/H2 Plasmas. *J. Vac. Sci. Technol., A* **2012**, *30* (4), 41303.

(46) Shoeb, J.; Kushner, M. J. Damage by Radicals and Photons during Plasma Cleaning of Porous Low-K SiOCH. II. Water Uptake and Change in Dielectric Constant. *J. Vac. Sci. Technol., A* **2012**, *30* (4), 41304.

(47) Cho, W.; Saxena, R.; Rodriguez, O.; Achanta, R.; Plawsky, J. L.; Gill, W. N. Effects of Sintering on Dielectric Constants of Mesoporous Silica. *J. Non. Cryst. Solids* **2004**, *350*, 336–344.

(48) Kurihara, K.; Ono, T.; Kohmura, K.; Tanaka, H.; Fujii, N.; Hata, N.; Kikkawa, T. Carbon Loss Induced by Plasma Beam Irradiation in Porous Silica Films. *J. Appl. Phys.* **2007**, *101* (11), 113301.

(49) Bao, J.; Shi, H.; Liu, J.; Huang, H.; Ho, P. S.; Goodner, M. D.; Moinpour, M.; Kloster, G. M. Mechanistic Study of Plasma Damage of Low K Dielectric Surfaces. *J. Vac. Sci. Technol. B Microelectron. Nanom. Struct.* **2008**, *26* (1), 219–226.

(50) Jung, H.; Park, J.; Yoo, E. S.; Han, G.-S.; Jung, H. S.; Ko, M. J.; Park, S.; Choe, W. Functionalization of Nanomaterials by Non-Thermal Large Area Atmospheric Pressure Plasmas: Application to Flexible Dye-Sensitized Solar Cells. *Nanoscale* **2013**, *5* (17), 7825–7830.

(51) Zen, S.; Ishibashi, Y.; Ono, R. Low-Temperature Sintering for Plastic Dye-Sensitized Solar Cells Using Conventional TiO2 Paste Containing Organic Binders. *Appl. Phys. Lett.* **2014**, *104* (21), 213904.